Met. Mater. Int., Vol. 16, No. 4 (2010), pp. 605~611
doi: 10.1007/s12540-010-0813-1 Published 26 August 2010

Pressureless Sintering of Nanocrystalline Hydroxyapatite at Different Temperatures

K. P. Sanosh[1,2], Min-Cheol Chu[2], A. Balakrishnan[3], T. N. Kim[1], and Seong-Jai Cho[2,*]

[1]Department of Information and Electronic Materials Engineering,
College of Engineering, Paichai University, Daejeon 302-735, Korea
[2]Division of Metrology for Emerging Technology, Korea Research Institute of Standards and Science,
1 Doryong-dong, Yuseong-gu, Daejeon 305-340, Korea
[3]Amrita Center for Nanosciences, Amrita Institute of Medical Sciences and Research Center,
Kochi 682026, Kerala, India

(received date: 11 May 2009 / accepted date: 16 June 2009)

In this work, the sintering behaviour of hydroxyapatite (HA) at different temperatures was studied. Nano HA powders synthesized by sol-gel technique were uniaxially pressed at 30 MPa into pellets and cold isostatically pressed at 200 MPa. The pellets were sintered in air at temperatures ranging from 900 ℃ to 1400 ℃ with a holding time of 2 h. It was observed that, at a sintering temperature of 1200 ℃ when the material was composed of pure HA phase, the samples exhibited densities of > 98.5 % of the theoretical value and possessed a hardness value of 5.89 GPa. Decomposition of HA into the secondary phases of TCP and CaO was found to occur at 1300 ℃ and 1400 ℃, respectively. Changes in the microstructure, relative density and hardness of the sintered HA ceramics with the sintering temperature were also analyzed. The variation in the hardness was found to be dependent on the relative density up to a threshold grain size limit of 2 μm. However, beyond this threshold, no correlation existed between the two properties. Porosity and grain size were found to play an important role in determining the properties of the sintered HA compacts.

Keywords: ceramics, sol-gel, grain growth, powder processing, sintering

1. INTRODUCTION

Hydroxyapatite ($Ca_{10}(PO_4)_6(OH)_2$ or HA) has been extensively investigated because it forms the main inorganic constituent of human bones and teeth [1]. The biocompatibility of HA is attributed to its calcium-to-phosphorus ratio being similar to that of natural bone and teeth, thus making it an ideal candidate for clinical applications [2-4]. HA has found success in hard tissue surgery [5], as it is capable of undergoing bonding osteogenesis and is relatively insoluble *in vivo*. However, its use has been limited to low load-bearing applications, because its mechanical properties are relatively poor [6,7] compared to other technical ceramics, such as alumina and zirconia. However, many attempts have been made to improve its mechanical properties by optimizing the processing, sintering regimes [8], and by controlling important parameters such as the particle size and shape, particle distribution and agglomeration [9], thereby obtaining high density. One of the recent approaches in obtaining high-density compacts is the use of finer HA particles [10]. During the sintering process, atoms migrate from the grain boundaries between the particles to the neck area, while the vacancies travel in the opposite direction to the material and are discharged at the surface of the material. As a result, the density of the material increases during sintering [11]. The finer the particle size, the faster is the motion of the atoms and the higher is the sintered density of the material at a given temperature [12]. Not only faster sintering occurs but also decomposition of HA into tricalcium phosphate (TCP) occurs at relatively high temperatures [13]. Thus, engineering HA at the nano level would give it superior functional properties due to its grain size and large surface-area-to-volume ratio and because its crystallinity would be similar to that of biological apatite [14]. Selection of a suitable sintering method is also a critical controlling parameter that requires attention during the processing of HA in order to obtain a solid, high-density HA body that is characterized by its fine-grained microstructure. Many sintering techniques [15-18] have proven to be effective in obtaining the desired density and mechanical properties for compact HA. However, considering the cost and degree of simplicity, the desirable sintering method

*Corresponding author: sjcho@kriss.re.kr

for HA is conventional pressureless sintering (CPS) in an air atmosphere. Hence, in the present work, the sintering behavior of nano HA powder synthesized by sol-gel method is studied using the CPS technique. HA pellets made by uniaxial compaction were pressureless-sintered in air at temperatures ranging from 900 °C to 1400 °C. The thermal and physical stability of the HA was assessed in terms of the phases present, densification behaviour and hardness. In addition, the effects of the grain size on the hardness of the sintered HA were also investigated.

2. EXPERIMENTAL PROCEDURE

In the present work, calcium nitrate tetrahydrate ($Ca(NO_3)_2 \cdot 4H_2O$) (CNT) (Junsei Chemicals Co., Ltd., S. Korea), phosphoric acid (H_3PO_4) (PA) (Samchun Pure Chemicals Co., Ltd, S. Korea) and ammonia (NH_3) (Daejung Chemicals and Metals Co. Ltd. S .Korea) were used as the starting precursors. 0.25 M PA was prepared in double distilled water. To this solution, ammonia was added and stirred until a constant pH of 10 was obtained. 1 M CNT was prepared by completely dissolving it in double distilled water. This CNT solution was slowly added to the above PA-ammonia solution, maintaining a Ca/P ratio of 1.67. The solution was kept constant at pH 10 by further adding small amounts of ammonia. The solution was rigorously stirred for 1 h and kept for ageing for 24 h at room temperature. The gel obtained after aging was dried at 65 °C for 24 h in a dry oven. The powders from the dried gel were washed repeatedly using double distilled water to remove NH_4^+ and NO_3^-. After washing, the powder was dried in air at 80 °C for 24 h. The morphology of the powder was determined by transmission electron microscopy (HR-TEM, Model Tecnai — Philips F30, FEI Co., Hillsboro, OR, USA). The particle size distribution (PSD) of the powder was obtained using a condensation particle counter (GRIMM Aerosol Technik, Gmbh, Germany (Serial No. 5400)). The phase purity of the powder was determined by Raman spectroscopy (KRISS Raman Spectrometer, Korea) The elemental composition of the powder was determined using energy dispersive x-ray (EDX) (ISI-DS130C, dual-stage SEM-EDX Akashi, Japan). The dried powders were uniaxially pressed at 30 MPa into pellets using a 10 mm cylindrical stainless steel die. The compacted green body was then cold-isostatically pressed (CIP) at 200 MPa. The CIP pellets were sintered in air at temperatures ranging from 900 °C to 1400 °C at a furnace ramp rate of 2 °C/min and a soaking time of 2 h. The linear shrinkage of the samples was determined by comparing the difference in the diameter of the green body and the sintered body. The density of the sintered samples (five for each condition) was determined by Archimedes' method using distilled water by taking the theoretical density of hydroxyapatite as 3.156 g cm^{-3}. The crystalline phases were identified by x-ray diffraction (XRD) (Bruker-axs, Germany). In addition, microstructural evolution under the various sintering temperatures was examined using scanning electron microscopy (SEM) (ISI-DS130C, Akashi, Japan). The samples were polished to a mirror surface finish using diamond paste and were subsequently etched with 0.1 % HF to delineate the grain boundaries. The average grain size (five each) was determined from scanning electron micrographs in a line intercept analysis with image analysis software (GMDH-USA). The hardness of the sintered compacts was measured using a Vickers microindentor (Matsuzawa DVK-25 Indenter, Japan) at a load of 1 kg (9.8 N) applied for 10 s on the polished surface. The average hardness value was taken from ten indentations made for each sintered sample.

The HA particle size, crystallinity and amount of secondary phases were calculated from XRD using Eqs. 1, 2, and 3, respectively.

$$D = \frac{0.89\lambda}{\beta \cos\theta} \tag{1}$$

where D is the particle size, λ is the wavelength (Cu Kα), β is the full width at the half-maximum of the HA (211) line and θ is the diffraction angle [19].

$$X_c = \frac{1 - \nu_{112/300}}{I_{300}} \tag{2}$$

where (X_c) is fraction of the crystalline phase, I_{300} is the intensity of the (300) diffraction peak and $V_{112/300}$ is the intensity of the hollow between the (112) and (300) diffraction peaks of HA [20].

$$V_{\text{sec } ondaryphase} = \frac{I_1 + I_2}{I_1 + I_2 + I_{HA}} \tag{3}$$

Here, I_{11} and I_2 are the intensities of the two strongest peaks of the secondary phase, and I_{HA} is the intensity of the strongest peak of the HA phase [21].

3. RESULTS AND DISCUSSION

The average measured amounts of Ca and P from the EDX analysis in the starting powder (3 samples) were determined as 67.81 wt.% and 32.19 wt.%, respectively. This gave a Ca/P molar ratio of 1.65 ± 0.02. This value was in close agreement with the ideal stoichiometric molar ratio value for pure HA of 1.667. The Raman spectroscopy analysis of the prepared HA powder (Fig. 1) revealed only peaks (OH^- and PO_4^{3-}) corresponding to the HA phase. The XRD pattern of the starting HA powder is shown in Fig. 2. The XRD analysis showed no secondary phases in the starting powder and was in agreement with the Raman spectroscopy result. The particle size calculated from Eq. 1 showed the presence of 20 nm HA particles in the starting powder. The crystallinity measured using Eq. 2 showed the powders to be of low crys-

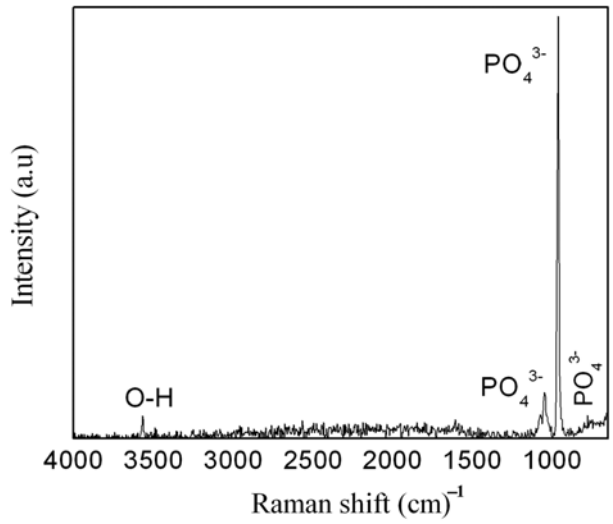

Fig. 1. Raman spectroscopy of synthesized nano HA powder showing characteristic peaks of OH^- and PO_4^{3-}.

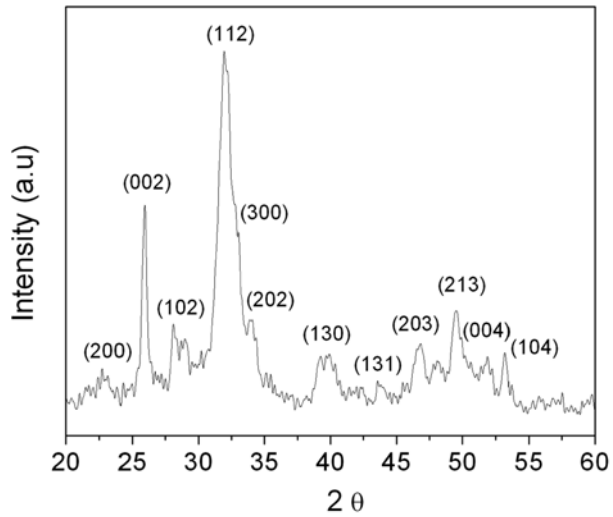

Fig. 2. XRD pattern of synthesized nano HA powder.

tallinity (~10 %).

Particle size distributions of the powder are shown in Fig. 3. The plot showed a narrow range of particle sizes and had a normal distribution. The average particle size was found to be centered at ~23 nm. TEM micrographs of the powder (Fig. 4) showed the presence of soft agglomerates in the nanometric range. The result of a phase analysis by XRD of the sintered samples is presented in Table 1.

The XRD pattern of the HA samples sintered at 1200 °C and below did not indicate the presence of any secondary phases (Fig. 5). The Ca/P molar ratio of the HA sintered at 1200 °C according to the EDX analysis gave a stoichiometric value (1.62 ± 0.07), indicating that the HA powders were thermally stable up to 1200 °C. Any large deviation from the stoichiometric value would have resulted in the formation of β-TCP, as observed at a temperature of 1400 °C. However,

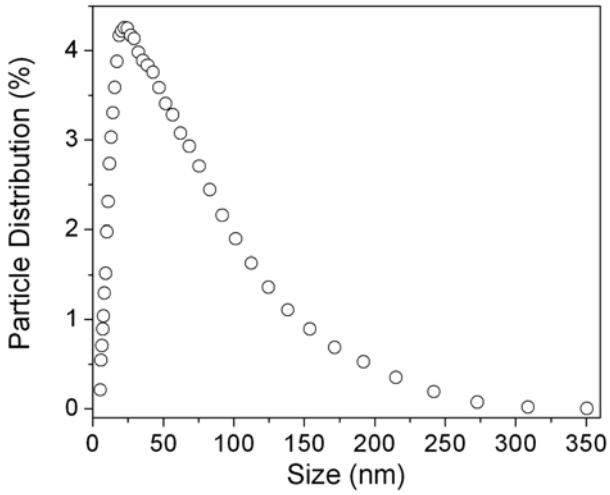

Fig. 3. Particle size distribution of synthesized nano HA powder.

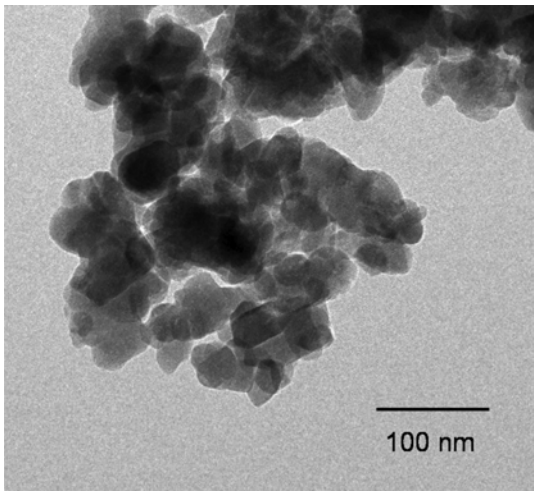

Fig. 4. TEM image of synthesized nano HA powder exhibiting the presence of soft agglomerates.

Table 1. Phases detected at room temperature in the HA samples when sintered at different temperatures

Temperature (°C)	HA (%)	Secondary phases (%)
900	100	-NA-
1000	100	-NA-
1100	100	-NA-
1200	100	-NA-
1300	~68	α-TCP (~32)
1400	~26	α-TCP (~56), β-TCP (~17), CaO (~1)

in the present case, the decomposition of HA at 1300 °C resulted in the formation of only α-TCP and hence could not be attributed to non-stoichiometric HA. It is believed that the decomposition of HA was associated with the formation of an intermediate phase, oxyapatite, that forms through the gradual loss of the radical OH^- (dehydroxylation) in the matrix when HA is heated in air to above 1200 °C. It has also been

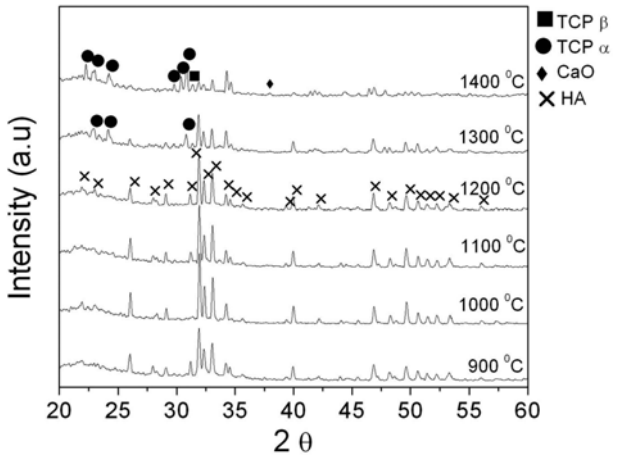

Fig. 5. X-ray diffraction patterns of HA sintered at different temperatures for 2 h.

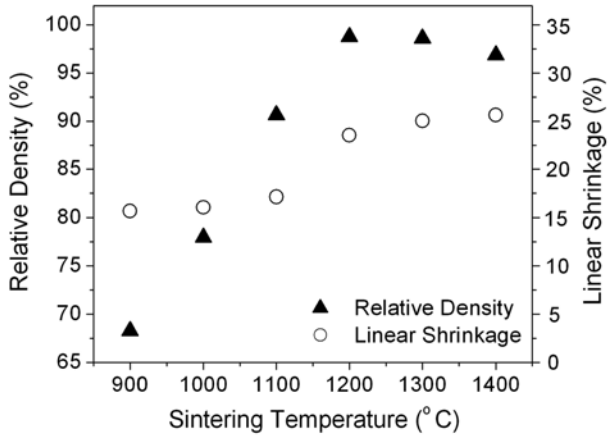

Fig. 6. Plot showing the variation in the relative density and linear shrinkage of HA ceramics with respect to the sintering temperature.

suggested that during heating, HA molecules tend to lose H_2O [22]; the formation of oxyapatite then occurs according to the following equation [23,24]:

$$2OH \rightarrow O + H_2O \quad (4)$$

$$Ca_{10}(PO_4)_6(OH)_2 \rightarrow Ca_{10}(PO_4)_6O^{\cdot}\square + H_2O \quad (5)$$

Here, □ is a non-charged vacancy and the hydroxyl ion-deficient product $Ca_{10}(PO_4)_6O^{\cdot}\square$ is known as oxyapatite [23]. Accordingly, one of the lattice sites which was originally occupied by two OH groups in a HA unit cell is now occupied by an oxygen atom while the other remains vacant. Zhou *et al.* [22] found that this oxyapatite phase is stable and will not undergo any reverse phase transformation. However, further heating could lead to HA decomposition to form β-TCP through the following process:

$$Ca_{10}(PO_4)_6(OH)_2 \rightarrow 2Ca_3(PO_4)_2 + Ca_4P_2O_9 + H_2O \quad (6)$$

The minor presence of CaO, which was detected by XRD in the present material when sintered at 1400 °C, can be attributed to an alternative decomposition route according to the following reaction [25,26]:

$$Ca_{10}(PO_4)_6(OH)_2 \rightarrow 3Ca_3(PO_4)_2 + CaO + H_2O \quad (7)$$

The effect of the sintering temperature on the relative density and linear shrinkage of HA is shown in Fig. 6. It was found that the linear shrinkage increases from ~15 % at 900 °C to 25 % at 1400 °C. A similar trend was also observed in the relative density plot, in which the measured density increased from 68 % (sintered at 900 °C) to 97 % (sintered at 1400 °C). The maximum densities of 98.76 % and 98.65 % were measured for samples sintered at 1200 °C and 1300 °C, respectively (Fig. 6). Both curves in Fig. 6 exhibit a sigmoidal trend with an inflexion point around 1200 °C. This point marks the temperature where maximum densification starts to take place. SEM examination of samples sintered below 1200 °C showed the presence of a large number of pores (Fig. 7)

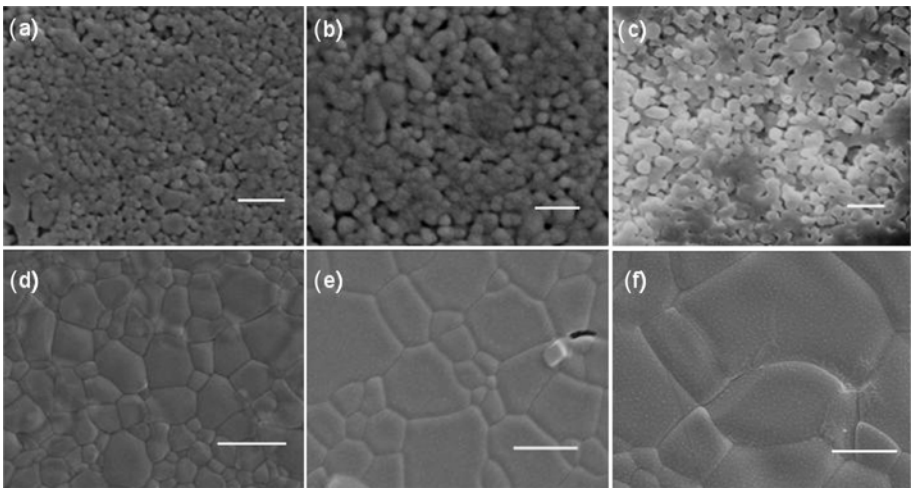

Fig. 7. SEM of polished and etched HA surfaces sintered at different temperatures (a) 900 °C, (b) 1000 °C (c) 1100 °C, (d) 1200 °C, (e) 1300 °C, and (f) 1400 °C. (Scale bar represents a-e: 500 nm; d-f: 5 μm).

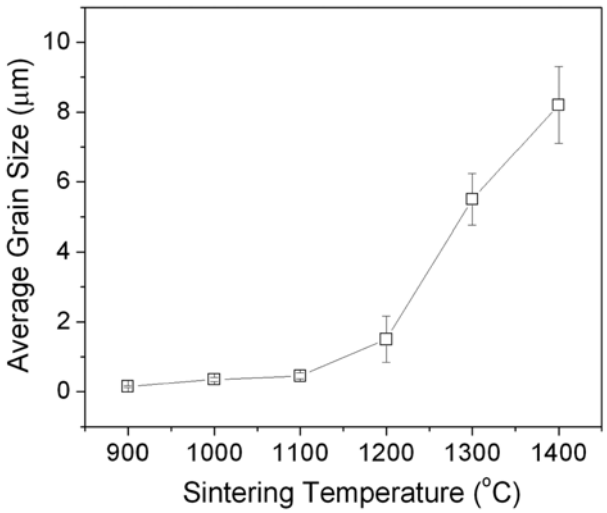

Fig. 8. Plot showing the variation in the average grain size of HA with respect to the sintering temperature.

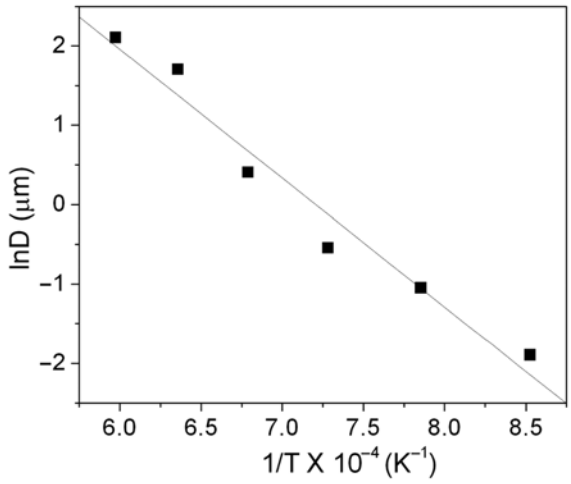

Fig. 9. Arrhenius plot of the log mean grain size vs. the reciprocal of the sintering temperature.

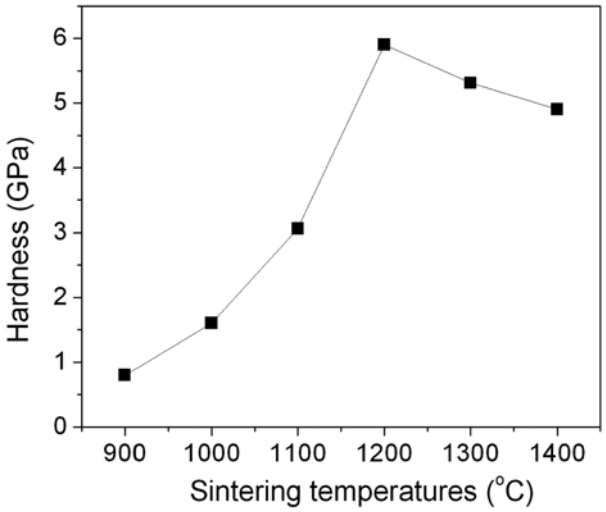

Fig. 10. Vickers hardness values of HA sintered at different temperatures.

which explained the low bulk density of this sample. In contrast, the slight decrease in the bulk density exhibited by samples sintered at 1300 °C and 1400 °C (Fig. 6) can be attributed to the decomposition of HA into secondary phases such as α, β TCP and CaO, as shown in Fig. 5 and Table 1.

In Fig. 8, the variation in the average grain sizes with the sintering temperature is presented. At temperatures of 1300 °C and 1400 °C, considerable grain growth occurred when compared to the sample sintered at 1200 °C. For instance, the average measured grain size of samples sintered at 1200 and 1400 °C were 1.5 ± 0.8 and 8.2 ± 1.1 μm, respectively. This represents an approximate five-fold increase in the grain size in this temperature range. The apparent activation energy for grain growth was determined from the grain size measurements by constructing an Arrhenius plot for a constant sintering time, as shown in Fig. 9. The best fit line was plotted using the least min square method. The slope of this line was used to determine the activation energy (Q) from the following equation [27]:

$$D = A\exp[-Q/RT] \quad (8)$$

In this equation, D is the average grain size, T is the temperature and R is the gas constant, i.e., 8.314 J/mol K. The value for Q obtained from this plot for grain growth in hydroxyapatite was 35 kcal/mol. There are many different Q values reported for HA, e.g., 34 kcal/mol [5], 36 kcal/mol [28], 47 kcal/mol [29], 56 kcal/mol [30] and 57 kcal/mol [25]. These discrepancies in the reported values compared to the present Q value can be attributed mainly to the difference in the particle size of the starting HA powder and the sintering schedule employed. It was found that as the size of the nanocrystals decreases [31,32]; the activation energy of atoms also decreases, thereby increasing the reactivity of the adjacent grains. In our case, the value of the activation energy, 35 kcal/mol, is much less than the other reported values [25,28-30] where the sintering of micronic and submicronic hydroxyapatite powders is considered.

The variation of the average Vickers hardness of samples sintered at various temperatures is shown in Fig. 10. Here, the lowest hardness value of 0.8 ± 0.073 GPa was measured for the sample sintered at 900 °C, whereas the maximum hardness value of 5.89 ± 0.28 GPa was obtained for the sample sintered at 1200 °C. The general trend, which can be observed from Fig. 10 is that, the hardness increases slowly from 900 °C to 1100 °C and then increases rapidly, almost doubling, when the temperature increases from 1100 °C to 1200 °C. However, a further increase in the temperature to >1200 °C resulted in a decrease in the hardness. The relatively low hardness obtained for samples sintered at temperatures below 1200 °C was possibly due to the low bulk

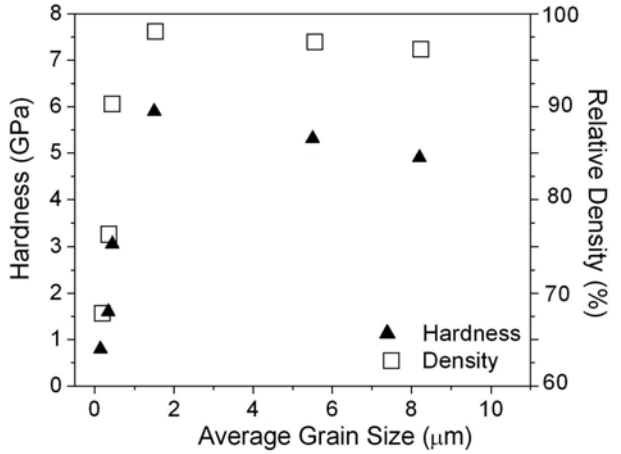

Fig. 11. Variation of the Vickers hardness and relative density as a function of the average grain size.

density of the material. The relationship between the grain size, relative density and hardness is shown in Fig. 11. Here, below ~2 μm the hardness trend correlates well with the change in the relative density; i.e., the hardness increases steadily with the relative density (Fig. 11). However, above 2 μm, the variation in the hardness did not appear to be in agreement with the density curve; i.e., the relative density was found to remain relatively constant at 97 % to 99 % while the hardness gradually decreased as the grain size increased. It appears that below some critical grain size e.g., (d_c) the hardness is governed by the bulk density (or porosity). In contrast, it is likely that above d_c=~2 μm, the bulk density is not the controlling parameter but rather the grain growth is. Another factor which could have, in part, contributed to the decline in the hardness after sintering at elevated temperatures (>1200 °C) is the decomposition of HA, which would have hindered the formation of strong inter-particle bonding in the ceramic matrix. Jarcho *et al*. [30] reported the presence of decomposition products at the grain boundaries of HA sintered in air at 1250 °C for 1 h. It was [33,34] also reported that the degradation of the mechanical properties in HA was due to the weakening of the grain boundary as a result of segregation of the decomposition product at the grain boundary regions. Hence, it appears that the presence of both secondary phases and larger grain sizes are detrimental to the densification and hardness of HA compacts.

4. CONCLUSIONS

In the present study, it was shown that the sintering temperature is a critical factor influencing the phase stability, densification behaviour, sintered microstructure and hence the hardness of HA. The optimum sintering temperature for HA was found to be 1200 °C with an average grain size of about 1.5 μm. A HA compact sintered at 1200 °C showed bulk density that exceeded 98.5 % and a maximum hardness value of 5.89 GPa. Sintering at lower temperatures (< 1200 °C) resulted in lower density and hardness. In contrast, the decrease in the density and hardness with an increase in the temperature (>1200 °C) was attributed to grain growth phenomenon above a critical size limit of 2 μm and decomposition of HA into secondary phases. The lower activation energy of HA (35 kcal/mol) in the present study can be attributed to the significant increase in the grain size at temperatures above 1200 °C.

REFERENCES

1. L. L. Hench, *J. Amer. Ceram. Soc.* **74**, 1487 (1991).
2. K. A. Khor and P. Cheang, *J. Mater. Proc. Technol.* **63**, 271 (1997).
3. K. A. Khor, P. Cheang, and Y. Wang, *JOM* **49**, 51 (1997).
4. H. S. Liu, T. S. Chin, L. S. Lai, S. Y. Chiu, K. H. Chung, C. S. Chang, and M. T. Chang, *Ceram. Int.* **23**, 19 (1997).
5. G. De With, J. A. Van Dijk, H. N. Hattu, and K. Prijs, *J. Mater. Sci.* **16**, 1592 (1981).
6. M. Akao, H. Aoki, and K. Kato, *J. Mater. Sci.* **16**, 809 (1981).
7. M. Ogiso, N. Nakabayashi, T. Matsumoto, M. Yamamura, and R. R. Lee, *J. Biomed. Mater. Res.* **30**, 109 (1996).
8. P. Siriphannon, Y. Kameshima, A. Yasumori, K. Okada, and S. Hayashi, *J. Eur. Ceram. Soc.* **22**, 511 (2002).
9. S. Best and W. Bonfield, *J. Mater. Sci.: Mater. Med.* **5**, 516 (1994).
10. A. Banerjee, A. Bandyopadhyay, and S. Bose, *Mater. Sci. Eng. C* **27**, 729 (2007).
11. N. Senamaud, D. Bernache-Assollant, E. Champion, M. Heughebaert, and C. Rey, *S. St. Ionics* **101-103**, 1357 (1997).
12. G. Georgiou and J. C. Knowles, *Biomaterials* **22**, 2811 (2001).
13. J. Y. Ying, S. E. Ahn, and A. Nakahira *US Patent 6013591* (2000).
14. R. Z. LeGeros, *Calcium Phosphates in Oral Biology and Medicine*, p. 154, H M Myers, Basel (1991).
15. B. Chen, T. Zhang, J. Zhang, Q. Lin, and D. Jiang, *Ceram. Int.* **34**, 359 (2008).
16. V. Jokanovic, B. Jokanovic, D. Markovic, V. Zivojinovic, S. Pasalic, D. Izvonar, and M. Plavsic, *Mater. Chem. Phys.* **111**, 180 (2008).
17. S. Ramesh, C. Y. Tan, S. B. Bhaduri, W. D. Teng, and I. Sopyan, *J. Mater. Process. Tech.* **206**, 221 (2008).
18. C. Shu, Y. Xianzhu, X. Zhangyin, X. Guohua, L. Hong, and Y. Kangde, *Ceram. Int.* **33**, 193 (2007).
19. E. Landi, A. Tampieri, G. Celotti, and S. Sprio, *J. Eur. Ceram. Soc.* **20**, 2377 (2000).
20. L. A. Azaroff, *Elements of X-ray Crystallography*, McGraw-Hill, New York (1968).
21. A. Balakrishnan, B. B. Panigrahi, M. C. Chu, K. J. Yoon, T. N. Kim, and S. J. Cho, *J. Mater. Res.* **22**, 2550 (2007).

22. J. Zhou, X. Zhang, J. Chen, S. Zeng, and K. De Groot, *J. Mater. Sci.: Mater. Med.* **4**, 83 (1993).
23. T. Kijima and M. Tsutsumi, *J. Am. Ceram. Soc.* **62**, 455 (1979).
24. A. Krajewski and A. Ravaglioli, *Bioceramics* **5**, 105 (1984).
25. K. Kamiya, T. Yoko, K. Tanaka, and Y. Fujiyama, *J. Mater. Sci.* **24**, 827 (1989).
26. J. Wu and T. Yeh, *J. Mater. Sci.* **23**, 3771 (1988).
27. R. E. Smallman and R. J. Bishop, *Metals and Materials: Science, Processes, Applications*, p. 83 Butterworth-Heinemann Ltd., Oxford (1995).
28. T. K. Chaki and P. E. Wang, *J. Mater. Sci.: Mater. Med.* **5**, 533 (1994).
29. P. Van Landuyt, F. Li, J. P. Keustermans, J. M. Streydio, F. Delannay, and E. Munting, *J. Mater. Sci.: Mater. Med.* **6**, 8 (1995).
30. M. Jarcho, C. H. Bolen, M. B. Thomas, J. Bobick, F. Kay, and R. H. Doremus, *J. Mater. Sci.* **11**, 2027 (1976).
31. M. F. El-Sayed and M. M. Sallam, *Egypt. J. Solids* **30**, 1 (2007).
32. Q. Jiang, S. H. Zhang, and J. C. Li, *Solid State* Commun. **130**, 581 (2004).
33. L. L. Hench and J. Wilson, *An Introduction to Bioceramics*, p. 152, World Scientific (1993).
34. P. E. Wang and T. K. Chaki, *J. Mater. Sci. Mater. Med.* **4**, 150 (1993).